IMU-based Smartphone-to-Vehicle Positioning

Johan Wahlström, Isaac Skog, *Member, IEEE*, Peter Händel, *Senior Member, IEEE*, and Arye Nehorai, *Fellow, IEEE*

***Abstract*—In this paper, we address the problem of using inertial measurements to position a smartphone with respect to a vehicle-fixed accelerometer. Using rigid body kinematics, this is cast as a nonlinear filtering problem. Unlike previous publications, we consider the complete three-dimensional kinematics, and do not approximate the angular acceleration to be zero. The accuracy of an estimator based on the unscented Kalman filter is compared with the Cramér-Rao bound. As is illustrated, the estimates can be expected to be better in the horizontal plane than in the vertical direction of the vehicle frame. Moreover, implementation issues are discussed and the system model is motivated by observability arguments. The efficiency of the method is demonstrated in a field study which shows that the horizontal RMSE is in the order of $0.5\,[m]$. Last, the proposed estimator is benchmarked against the state-of-the-art in left/right classification. The framework can be expected to find use in both insurance telematics and distracted driving solutions.**

***Index Terms*—Insurance telematics, driver distraction, inertial sensors, centripetal acceleration, nonlinear filtering.**

I. Introduction

There is a steadily growing interest in smartphone-based traffic data collection. Today, smartphones are used for purposes of for example navigation [1], traffic state estimation [2], vehicle condition monitoring [3], and driver assistance [4]. Smartphone-based measurement systems benefit not only from their versatile set of sensors, typically including both a global navigation satellite systems (GNSS) receiver and an inertial measurement unit (IMU), but also from their low cost, transparency, and ease of use [5]. The need to estimate the position of a smartphone with respect to a vehicle (see Fig. 1) can arise for two reasons. First, the position of the smartphone can be used as one of many possible features that provide information about a driving trip. An accurate point estimate of the smartphone's position could for example help answer questions such as "Who is most likely to have driven the vehicle?". This is particularly relevant for the industry of smartphone-based insurance telematics where vehicle data, collected using smartphones, is used to adjust premiums and provide driver feedback [6]. In insurance telematics, the insurer can for example use GNSS measurements to infer the vehicle's position, or use IMU measurements to detect harsh braking. Typically, a substantial amount of statistical signal processing is required to enhance and monitor the quality of the data [7]. Second, the position of the smartphone can be used to minimize driver distraction by enabling location-dependent limitations of smartphone functionality while driving. This idea is utilized in apps such as DriveID, which uses patented Bluetooth technology to infer which side (right or left) of the car that the smartphone is placed in, and then locks the smartphone whenever it is on the driver's side during vehicle movement. While the classification of the smartphone's side in the vehicle is rather accurate, the cost of the required Bluetooth-equipped device is almost $100, thereby limiting the possibilities for large-scale deployment.

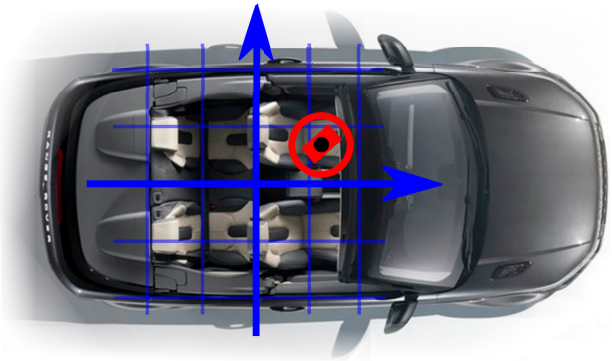

Fig. 1. Illustration of the problem of smartphone-to-vehicle positioning.

A. Smartphone-to-vehicle Positioning - State-of-the-art

Many modern cars can perform smartphone-to-vehicle positioning (or the closely related task of driver identification) by utilizing original equipment manufacturer (OEM)-technology based on e.g., Bluetooth and audio ranging [8], [9], voice recognition [10], or near-field communication [11]. Although these systems typically work very well, full market penetration is not expected within the near future, and aftermarket installations are often expensive. As a consequence, several low-cost methods for smartphone-to-vehicle positioning have been proposed. One alternative is to detect human motions using the smartphone's IMU and thereby try to infer the owner's seat in the vehicle. Studied motions have included vehicle entries [12], seat-belt fastening, and pedal press [11]. The exact patterns of the two former motions will typically differ depending on which side of the vehicle that the user entered from. Similarly, the detection of pedal press always indicates that the user sat in the driver's seat. While these features possess some predictive power, they are susceptible to variations in the motion behavior of each individual. In addition, they are constrained by the assumption that the user carries the smartphone in his pocket. Another option is to estimate the relative position of two spatially separated devices

J. Wahlström, I. Skog, and P. Händel are with the ACCESS Linnaeus Center, Dept. of Signal Processing, KTH Royal Institute of Technology, Stockholm, Sweden. (e-mail: {jwahlst, skog, ph}@kth.se).

A. Nehorai is with the Preston M. Green Department of Electrical and Systems Engineering, Washington University in St. Louis, MO 63130 USA (e-mail: nehorai@ese.wustl.edu).

The work of A. Nehorai was supported by AFOSR Grant No. FA9550-11-1-0210.

from their GNSS measurements. However, since the errors normally are heavily correlated in time and often exceed the typical device distance, convergence can be expected to be slow [13]. It is also possible to perform driver identification by studying individual driving styles and travel behaviors [14].

In this study, our focus will be on using that the specific force, measured by smartphone-embedded accelerometers, varies with smartphone's position in the vehicle. The effect is most clearly seen during high-dynamic events. For example, in [12] and [15] the relative longitudinal placement of two smartphones was inferred by comparing their accelerometer measurements when the vehicle passed a pothole. Similarly, in [15] and [16], the lateral placement of two smartphones was inferred from their centripetal acceleration. The acceleration was computed under the assumption that the vehicle's angular velocity was constant (i.e., that the angular acceleration was zero) and only nonzero along the yaw axis of the vehicle frame. In the following section, we will generalize this method by considering the complete three-dimensional kinematic relation between the specific forces. Thereby, the previously employed assumptions on the angular velocity are avoided. Obviously, the proposed method may be used in conjunction with any of the previously mentioned methods utilizing e.g., human motions, GNSS measurements, driving styles, etc.

B. Implementation Challenges

The presented estimation framework requires access to measurements from at least one gyroscope triad and at least two spatially separated accelerometer triads. Hence, if each smartphone is equipped with a 6-degrees of freedom IMU, we either need measurements from at least two smartphones, or from at least one smartphone and one external vehicle-fixed accelerometer triad. Since we are estimating the relative positions of the accelerometer triads, absolute positioning within the vehicle is typically only possible in the latter case and under the assumption that the absolute position of the external accelerometer triad is known. However, accurate estimates of relative positions are often sufficient input for reliable driver classifications, i.e., determining which of the smartphones that belongs to the driver (assuming that such a smartphone exists). Technical solutions where smartphone sensors are enhanced with external accelerometer triads [17], embedded into tags or on-board-diagnostics (OBD)-dongles, is currently utilized by telematics providers such as *Cambridge Mobile Telematics* and *Mojio*. The cost of a mass-produced accelerometer triad can be expected to be less than half a dollar [18], and hence, the cost of producing and installing an accelerometer tag is typically negligible.

C. Insurance Telematics

Now, we go into more detail on the practical use of smartphone-to-vehicle positioning within insurance telematics. While most automotive insurances follow the vehicle, data collected using a smartphone normally follows the user. (Since most insurance telematics apps are implemented with an autostart feature, data will be sent to the insurer whenever the smartphone is situated in a motor vehicle [19].) Generally, this will cause issues of data association. For example, we can imagine scenarios where you lend your car to someone who is not a registered driver within your telematics policy (data will be lost), or where you take a cab or ride along in a friend's car (data can be mistaken as having emerged from a trip with your car). In the latter case, smartphone-to-vehicle positioning might be used to detect which trips that were made with a third party vehicle. More specifically, one would use that the probability that the trip was made with the insured car is higher conditioned on that the data was recorded from the driver's seat and vice versa.

One practical issue is that of data sharing, i.e., even if there are multiple smartphones in a vehicle they might not be configured to neither share data in real-time nor send data to the same server [20]. Moreover, problems could arise due to the implicit assumption that the smartphone is placed in the vicinity of its user. Installing an accelerometer tag solves the issues of data association (data from the tag immediately reveals whether the insured vehicle was driven) and of data sharing (the insurer will have access to data from both the tag and the smartphone-embedded accelerometer). Even though the problem of data association would be solved by the use of tags, there would still be reasons to be interested in identifying the driver in each trip. For example, this information could be used to confirm accident reports where the insurance coverage differs depending on who was driving during the accident (liability insurance often follows the driver). For discussions on privacy in mobile sensing applications, refer to [21].

D. Outline

In this article, we examine the possibilities of using IMU measurements to position a smartphone with respect to a vehicle. The achievable accuracy is evaluated with both simulations and experimental data. The basis of the proposed estimation framework is presented in Section II. Section III studies parametric Cramér-Rao bounds (CRBs) using both numerical and analytical methods. Subsequently, Section IV presents the results of the conducted field study. Last, Section V summarizes the study.

Reproducible research: The experimental data used in this paper is available at www.kth.se/profile/jwahlst/ together with a Matlab implementation of the proposed method.

II. Model and estimation framework

Consider a moving vehicle with one gyroscope triad and N accelerometer triads. All sensors are assumed to be fixed to the vehicle. Our aim will be to fuse the measurements from the gyroscopes and the accelerometers to estimate the relative positions of the accelerometer triads in the vehicle frame. We begin by presenting kinematic and dynamic models for the vehicle, and then describe the sensor model. Following this, the estimation problem is formulated as a nonlinear filtering problem where the vehicle dynamics and the sensor biases are treated as nuisance parameters. Last, relevant filtering methods are reviewed and the observability properties of the presented system are analyzed.

A. Kinematic Model

Let us, without loss of generality, order the accelerometer triads from 1 to N and define the origin of the vehicle frame to be at the position of the first accelerometer triad. It then holds that [22]

$$\mathbf{a}^{(n)} = \mathbf{a}^{(1)} + ([\boldsymbol{\omega}]^\times[\boldsymbol{\omega}]^\times + [\boldsymbol{\alpha}]^\times)\mathbf{r}^{(n)} \tag{1}$$

where $\mathbf{a}^{(n)}$ and $\mathbf{r}^{(n)}$ denote the specific force and the position in the vehicle frame of the nth accelerometer triad, respectively. Further, $\boldsymbol{\omega}$ and $\boldsymbol{\alpha}$ denote the vehicle's angular velocity and acceleration with respect to inertial space, respectively. The skew symmetric matrix $[\mathbf{c}]^\times$ is defined such that $[\mathbf{c}_1]^\times\mathbf{c}_2$ is equal to the cross product of $\mathbf{c}_1$ and $\mathbf{c}_2$.

B. Dynamic Model

The dynamics of the vehicle are modeled according to

$$\boldsymbol{\omega}_{k+1} = \boldsymbol{\omega}_k + \Delta t\,\boldsymbol{\alpha}_k, \tag{2a}$$
$$\boldsymbol{\alpha}_{k+1} = \boldsymbol{\alpha}_k + \mathbf{w}_{\alpha,k}. \tag{2b}$$

Here, Δt denotes the sampling interval and we are using the subindex k to denote quantities at sampling instance k. Further, the noise term $\mathbf{w}_{\alpha,k}$ is assumed to be normally distributed and white with covariance $\Delta t\,\sigma_\alpha^2\,\mathbf{I}_3$, where $\mathbf{I}_\ell$ denotes the identity matrix of dimension ℓ.

C. Sensor Model

The measurements from the gyroscope triad and the nth accelerometer triad are modeled as

$$\widetilde{\boldsymbol{\omega}}_k = \boldsymbol{\omega}_k + \mathbf{b}_{\omega,k} + \boldsymbol{\epsilon}_{\omega,k}, \tag{3a}$$
$$\tilde{\mathbf{a}}_k^{(n)} = \mathbf{a}_k^{(n)} + \mathbf{b}_{a,k}^{(n)} + \boldsymbol{\epsilon}_{a,k}^{(n)}, \tag{3b}$$

where $\boldsymbol{\epsilon}_{\omega,k}$ and $\boldsymbol{\epsilon}_{a,k}^{(n)}$ are normally distributed white noise processes with covariances $\sigma_\omega^2\,\mathbf{I}_3$ and $\sigma_a^2\,\mathbf{I}_3$, respectively. Further, (3) includes gyroscope and accelerometer biases which are assumed to develop according to the random walk models

$$\mathbf{b}_{\omega,k+1} = \mathbf{b}_{\omega,k} + \mathbf{w}_{\omega,k}, \tag{4a}$$
$$\mathbf{b}_{a,k+1}^{(n)} = \mathbf{b}_{a,k}^{(n)} + \mathbf{w}_{a,k}^{(n)}. \tag{4b}$$

Here, $\mathbf{w}_{\omega,k}$ and $\mathbf{w}_{a,k}^{(n)}$ are assumed to be normally distributed white noise processes with covariances $\Delta t\,\sigma_{b,\omega}^2\,\mathbf{I}_3$ and $\Delta t\,\sigma_{b,a}^2\,\mathbf{I}_3$, respectively.

D. State-space Model

Using (1) – (4), the vehicle dynamics and the measurements can be described by the state-space model

$$\mathbf{x}_{k+1} = \mathbf{f}(\mathbf{x}_k) + \mathbf{w}_k, \tag{5a}$$
$$\mathbf{y}_k = \mathbf{h}(\mathbf{x}_k) + \boldsymbol{\epsilon}_k. \tag{5b}$$

The state vector is defined as[1]

$$\mathbf{x} \triangleq \begin{bmatrix}\mathbf{r}^\mathsf{T} & \boldsymbol{\omega}^\mathsf{T} & \boldsymbol{\alpha}^\mathsf{T} & \mathbf{b}_\omega^\mathsf{T} & \delta\mathbf{b}_a^\mathsf{T}\end{bmatrix}^\mathsf{T} \tag{6}$$

[1]The choice of variables to include in $\mathbf{x}$ is motivated by the observability properties of the corresponding system. This is discussed in more detail in Section II-H.

where it has been used that $\mathbf{r} \triangleq \begin{bmatrix}(\mathbf{r}^{(2)})^\mathsf{T} & \dots & (\mathbf{r}^{(N)})^\mathsf{T}\end{bmatrix}^\mathsf{T}$, $\delta\mathbf{b}_a \triangleq \begin{bmatrix}(\delta\mathbf{b}_a^{(2)})^\mathsf{T} & \dots & (\delta\mathbf{b}_a^{(N)})^\mathsf{T}\end{bmatrix}^\mathsf{T}$, and $\delta\mathbf{b}_a^{(n)} \triangleq \mathbf{b}_a^{(n)} - \mathbf{b}_a^{(1)}$. It can be noted that $\mathbf{r}$ defines the relative position of any two accelerometer triads. Using (2) and (4), the state transition model can be shown to be linear, i.e., $\mathbf{f}(\mathbf{x}_k) \triangleq \mathbf{F}\mathbf{x}_k$, where $\mathbf{F}$ is defined as

$$\mathbf{F} \triangleq \mathbf{I}_{6N+3} + \begin{bmatrix}\mathbf{0}_{3(N-1),3N} & \mathbf{0}_{3(N-1),3} & \mathbf{0}_{3(N-1),3N} \\ \mathbf{0}_{3,3N} & \Delta t\,\mathbf{I}_3 & \mathbf{0}_{3,3N} \\ \mathbf{0}_{3(N+1),3N} & \mathbf{0}_{3(N+1),3} & \mathbf{0}_{3(N+1),3N}\end{bmatrix}. \tag{7}$$

We have here used $\mathbf{0}_\ell$ and $\mathbf{0}_{\ell_1,\ell_2}$ to denote zero matrices of dimensions $\ell \times \ell$ and $\ell_1 \times \ell_2$, respectively. Similarly, it can be shown that $\mathbf{w}_k$ is normally distributed and white with covariance $\mathbf{G}\mathbf{Q}\mathbf{G}^\mathsf{T}$ where

$$\mathbf{Q} \triangleq \Delta t \cdot \mathrm{blkdiag}(\sigma_\alpha^2\,\mathbf{I}_3, \sigma_{b,\omega}^2\,\mathbf{I}_3, \sigma_{b,a}^2\,\bar{\mathbf{I}}_{N,3}), \tag{8a}$$
$$\mathbf{G} \triangleq \begin{bmatrix}\mathbf{0}_{3(N+1),3N} & \mathbf{I}_{3(N+1)}\end{bmatrix}^\mathsf{T}, \tag{8b}$$

and $\bar{\mathbf{I}}_{n,m} \triangleq (\mathbf{I}_{n-1} + \mathbb{1}_{n-1}) \otimes \mathbf{I}_m$. Here, $\mathrm{blkdiag}(\cdot,\dots,\cdot)$ denotes the block diagonal matrix with block matrices given by the arguments, $\mathbb{1}_\ell$ denotes the matrix of dimension $\ell \times \ell$ with all elements equal to one, and $\otimes$ denotes the Kronecker product. Now, defining $\delta\tilde{\mathbf{a}}^{(n)} \triangleq \tilde{\mathbf{a}}^{(n)} - \tilde{\mathbf{a}}^{(1)}$ and $\mathbf{h}^{(n)}(\mathbf{x}) \triangleq \delta\mathbf{b}_a^{(n)} + ([\boldsymbol{\omega}]^\times[\boldsymbol{\omega}]^\times + [\boldsymbol{\alpha}]^\times)\mathbf{r}^{(n)}$, equations (1) and (3) yield the measurement vector and the measurement function

$$\mathbf{y} \triangleq \begin{bmatrix}\widetilde{\boldsymbol{\omega}}^\mathsf{T} & (\delta\tilde{\mathbf{a}}^{(2)})^\mathsf{T} & \dots & (\delta\tilde{\mathbf{a}}^{(N)})^\mathsf{T}\end{bmatrix}^\mathsf{T}, \tag{9a}$$
$$\mathbf{h}(\mathbf{x}) \triangleq \begin{bmatrix}\boldsymbol{\omega}^\mathsf{T} & (\mathbf{h}^{(2)}(\mathbf{x}))^\mathsf{T} & \dots & (\mathbf{h}^{(N)}(\mathbf{x}))^\mathsf{T}\end{bmatrix}^\mathsf{T}, \tag{9b}$$

respectively. Moreover, it follows that $\boldsymbol{\epsilon}_k$ will be a normally distributed white noise process with covariance $\mathbf{R} \triangleq \mathrm{blkdiag}(\sigma_\omega^2\,\mathbf{I}_3,\, \sigma_a^2\,\bar{\mathbf{I}}_{N,3})$. It can be noted that the measurement vector (9a) includes the difference in the measurements from $N-1$ specific pairs of accelerometer triads. The same information can be provided to the system by including the measurement difference of any $N-1$ pairs of accelerometer triads, as long as all accelerometer triads appear at least once in the total set of pairs. Any measurement defined by an additional Nth pair of accelerometer triads can be obtained as a linear combination of the measurements defined by the original $N-1$ pairs, and is therefore redundant.

E. Filters for Nonlinear Systems

Due to the nonlinearity of the system (5), no optimal (in mean-square sense) and finite-dimensional estimator of $\mathbf{x}$ is available, and we will have to resort to suboptimal implementations. A large number of suitable estimators have been described in the literature. If the nonlinearities are not too severe, we may linearize the system around the current estimate and then apply the optimal estimator of the resulting approximate linear model. This defines the extended Kalman filter (EKF) [23]. A popular alternative to the EKF is the unscented Kalman filter (UKF). As shown in [24], the UKF outperforms the EKF in most circumstances. In this study, we will be confined to UKF-based implementations.

Typically, an UKF has a computational cost in the same order as that of the corresponding EKF. In the most straightforward implementation, this computational cost is dominated by a term in the order of $6d^3$ per iteration, where $d = 6N+3$

denotes the dimension of the state vector [25]. Hence, running the algorithm with e.g., $N = 3$ at $20\,[Hz]$ would require $20 \cdot 6 \cdot 21^3\,[flops] \approx 1.1\,[Mflops]$, which is several orders of magnitude smaller than the maximum number of flops performed by standard smartphones [26].

If particle-based implementations are considered, it can be noted that the system is conditionally linear in both the positions $\mathbf{r}$ and the bias terms $\mathbf{b}_\omega$ and $\delta\mathbf{b}_a$. Hence, it suffices to employ a marginalized particle filter (MPF) where only the posteriors of the vehicle dynamics $\boldsymbol{\omega}$ and $\boldsymbol{\alpha}$ need to represented by particles [27].

F. Classification

Once a position estimate have been obtained, it is easy to e.g., make left/right or front/back classifications, perform hypothesis tests, or compute uncertainty ellipses by employing a Gaussian approximation. Here, a left/right (front/back) classification refers to the process of determining which of two devices that is the closest to the left/right (front/back) side of the vehicle. As an example, assume that we have processed all available measurements with $N = 2$ and that the final position estimate is $\hat{\mathbf{r}}$ with the associated filter covariance $\boldsymbol{\Sigma}_r$. We will then consider the first accelerometer to be placed on the right side of the second accelerometer if and only if $\hat{r}_{lat}$, i.e., the element of $\hat{\mathbf{r}}$ indicating position in the lateral direction of the vehicle frame (with the lateral axis pointing to the right in the vehicle), is negative. Similarly, the generalized likelihood ratio for testing the hypothesis that the first accelerometer is on the right side of the second accelerometer is $\Lambda = p_{\mathcal{N}}(\max(\hat{r}_{lat}, 0), \sigma^2_{lat})/p_{\mathcal{N}}(0, \sigma^2_{lat})$ [28], where $p_{\mathcal{N}}(\,\cdot\,, \sigma^2)$ denotes the probability density function of a normal distribution with zero mean and variance σ^2, while σ^2_{lat} denotes the diagonal element of $\boldsymbol{\Sigma}_r$ associated with the lateral direction.

G. Distributed Filtering

If the estimation is to be performed in real-time with no dependence on OEM infrastructure, the computations must be done directly on the relevant smartphones or on vehicle-installed devices (e.g., tags). This calls for implementations utilizing distributed filtering. However, since the length of the state vector exceeds the number of the measurements obtained per filter iteration, less communications are generally required when transmitting measurements than when transmitting estimation statistics. Hence, a feasible alternative is to employ a centralized leader-agent solution, where all measurements are sent to a single processing node (the leader-agent), which then performs the filter iterations [29]. Obviously, the choice of leader-agent may vary with time.

H. Observability

We will address issues related to the observability of (5) by studying the observability properties of the corresponding linear system. (This is a common approach for systems which are not subject to e.g., multimodal or discontinuous error distributions [30].) The linearized system is said to be observable over the interval $[t_1, t_k]$ if and only if the rank of the observability matrix $\mathbf{O}_{1,k} \triangleq \left[\mathbf{H}_1^\intercal \;\; (\mathbf{H}_2\mathbf{F})^\intercal \ldots (\mathbf{H}_k\mathbf{F}^{k-1})^\intercal\right]^\intercal$ is equal to the dimension of $\mathbf{x}$ [31]. Here, $\mathbf{H} \triangleq \partial\mathbf{h}(\mathbf{x})/\partial\mathbf{x}$ denotes the linearized measurement matrix. Normally, observability is attained already for small k in all but degenerate cases where e.g., the angular velocities and accelerations only are nonzero in one spatial dimension.

Several additional remarks can be made regarding the observability of the system and the chosen system model. For example, we note that the presented framework easily can be extended to include measurements from multiple gyroscope triads. A straightforward observability analysis shows that each separate gyroscope bias can be made observable. However, if the measurement noises of different gyroscope triads are assumed to be independent and identically distributed, it is usually more convenient to average the measurements before they are fed to the filter, and then only estimate the average bias. Moreover, notice that neither the vehicle's specific force nor any absolute accelerometer bias has been included in the state vector. To investigate this further, imagine that we extend the state vector with the specific force and the accelerometer bias at the first the accelerometer triad, and model both quantities to develop according to a random walk. (Obviously, it suffices to extend the state vector with the specific force and the accelerometer bias at the first the accelerometer triad to implicitly estimate the corresponding quantities at any accelerometer triad.) It is then easily confirmed that these quantities are mutually unobservable, even if (3b) is included in the measurement equation for $n = 1$. (Both quantities only enter the observability matrix through this measurement, and do so linearly.) However, if the bias or the specific force is known at an arbitrary accelerometer triad, this will make both quantities observable.

III. The Cramér-Rao Bound

Given some statistical estimation problem, the CRB provides a lower limit on the mean square estimation error of any unbiased estimator. There are two primary reasons to study this bound. First, it can be used to evaluate the performance of suboptimal estimators. If the mean-square error of an estimator is in the vicinity of the bound, the estimator is typically considered to be adequate. Second, it may help to discover inherent limitations of the problem at hand, or give hints on how to design experiments to increase estimator performance. In this section, we will make use of both these traits.

A. Definitions and Setup for Studies of the Parametric CRB

For a system model such as (5), both parametric and posterior CRBs are available. To make sure that we are able to capture all the characteristics of real-world vehicle dynamics, our focus will be on the parametric CRB, using dynamics from real-world data. (The same approach has previously been taken in e.g., [32].) This bound considers the classical framework with deterministic and unknown parameters, and must therefore be given with respect to some specified realization of the relevant state elements. Since the parametric CRB for the system model (5) is given by the Riccati recursion for

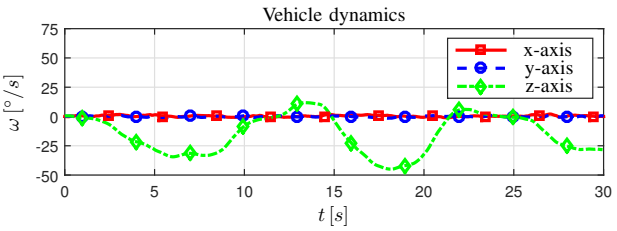

Fig. 2. The angular velocity along the x-axis (roll), y-axis (pitch), and z-axis (yaw) in a subset of the employed data set.

the covariance in the extended Kalman filter (where the state-space model is linearized around the true realization), it will suffice to specify realizations of $\mathbf{r}$, $\boldsymbol{\omega}$, and $\boldsymbol{\alpha}$ (the linearized filter matrices only depend on these state elements).

For ease of illustration, we will reduce the Cramér-Rao inequality to scalar form, and compare the empirical scalar root-mean-square error (RMSE) of the position errors with the trace of the corresponding submatrix of the inverse Fisher information matrix (FIM). The inequality can be written as [33]

$$\sqrt{\frac{1}{M}\sum_{i=1}^{M}\|\hat{\mathbf{r}}_i-\mathbf{r}\|^2} \gtrsim \sqrt{\mathrm{tr}(\mathbf{P}_r)} \tag{10}$$

and holds for each sampling instance (the time dependence has been suppressed for brevity). Here, M denotes the total number of simulations over the complete realization, $\|\cdot\|$ denotes the Euclidean norm, $\hat{\mathbf{r}}_i$ denotes the estimated relative positions during simulation i, $\mathbf{P}_r$ denotes the submatrix of the inverse FIM providing the lower bound on mean-square error of $\hat{\mathbf{r}}$, $\mathrm{tr}(\mathbf{A})$ denotes the trace of some matrix $\mathbf{A}$, and $\gtrsim$ denotes inequality in the limit of $M \to \infty$. For ease of notation, we define

$$\mathrm{RMSE}(\hat{\mathbf{r}}) \triangleq \frac{1}{\sqrt{\dim(\mathbf{r})}}\sqrt{\frac{1}{M}\sum_{i=1}^{M}\|\hat{\mathbf{r}}_i-\mathbf{r}\|^2} \tag{11a}$$

and

$$\mathrm{CRB}(\mathbf{r}) \triangleq \frac{1}{\sqrt{\dim(\mathbf{r})}}\sqrt{\mathrm{tr}(\mathbf{P}_r)}. \tag{11b}$$

Here, $\dim(\mathbf{r}) \triangleq 3(N-1)$ is the length of the vector $\mathbf{r}$. The factor $1/\sqrt{\dim(\mathbf{r})}$ has been included to facilitate a comparison between scenarios with a different number of accelerometers.

B. Simulation-based Evaluation of the UKF

Inertial data was collected from a Microstrain 3DM-GX3-35 placed in a vehicle performing harsh cornering maneuvers. It should be intuitively clear already from equation (1) that a certain level of angular rotation (e.g., cornering) is required to estimate the relative positions. This is discussed in more detail in Section III-C. The data included 32 cornering maneuvers collected over approximately 6 minutes on an empty parking lot. The sampling rate was $20\,[Hz]$. Fig. 2 serves to illustrate the studied dynamics (the true dynamics provided by the reference system) by showing a 30-second snippet of the vehicle's angular velocity.

TABLE I
SIMULATION PARAMETERS.

	Parameter	Value
Positions†	$\mathbf{r}^{(2)}$	$[0\ \ 1\ \ 0.5]\,[m]$
	$\mathbf{r}^{(3)}$	$[1\ \ 0\ \ 0.5]\,[m]$
	$\mathbf{r}^{(4)}$	$[1\ \ 1\ \ 1]\,[m]$
Sensor noise	σ_ω	$1\,[^\circ/s]$
	σ_a	$0.035\,[m/s^2]$
Bias drift	$\sigma_{b,\omega}$	$0.0015\,[^\circ/s^2/\sqrt{Hz}]$
	$\sigma_{b,a}$	$5\cdot10^{-5}\,[m/s^3/\sqrt{Hz}]$
Dynamics	σ_α	$8\,[^\circ/s^3/\sqrt{Hz}]$

† The positions are given along the vehicle's longitudinal, lateral, and up direction, respectively.

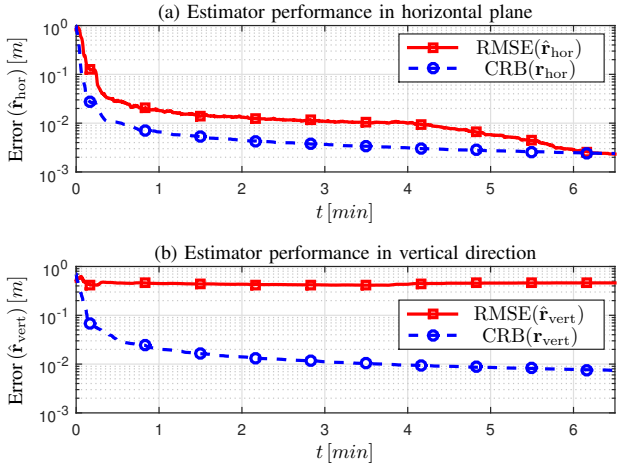

Fig. 3. The (a) horizontal and (b) vertical RMSE of the UKF evaluated against the CRB.

The simulation parameters are given in Table I. As can be seen, the simulated measurements were assumed to be gathered from four 6-degrees of freedom IMUs, placed in the corners of a rhombus. Further, the RMSEs were computed from $M = 100$ simulations using a standard UKF implementation [23]. In each simulation run, we generated constant accelerometer and gyro biases from uniform distributions in the intervals of $(-0.5, 0.5)\,[m/s^2]$ and $(-0.25, 0.25)\,[^\circ/s]$, respectively. See [22], [34], [35] for typical bias values. The angular velocity and acceleration were initialized from the measurements, and the relative positions and the bias terms were initialized as zero.

As the larger part of the angular velocity and the angular acceleration was along the yaw axis of the vehicle frame (as is typical for vehicle dynamics), the errors of the estimated relative position will also be larger in this direction. (Note that $\mathbf{r}^{(n)}$ is locally unobservable in the direction of $\boldsymbol{\omega}$ as long as $\boldsymbol{\omega}$ and $\boldsymbol{\alpha}$ are parallel and constant.) To illustrate the resulting effect on the estimates, we study the horizontal (along the longitudinal and lateral dimensions of the vehicle frame) and vertical (in the up direction of the vehicle frame) contributions to $\mathrm{RMSE}(\hat{\mathbf{r}})$ and $\mathrm{CRB}(\mathbf{r})$ separately. For example, when studying the horizontal $\mathrm{RMSE}(\hat{\mathbf{r}})$, only the lateral and longitudinal elements of $\mathbf{r}$ were considered in (11a).

Fig. 3 (a) and (b) show the CRB together with the RMSE for the horizontal position estimates $\hat{\mathbf{r}}_{\text{hor}}$ and vertical position estimates $\hat{\mathbf{r}}_{\text{vert}}$, respectively. As can be seen in Fig. 3 (a), the estimates of relative position reach decimeter-level accuracy in the horizontal plane after about twelve seconds (corresponding to one cornering maneuver). The CRB is attained after about six minutes. By contrast, Fig. 3 (b) shows that the estimates do not converge in the vertical direction. However, it should be noted that it is unclear whether the CRB is attainable at all. Either way, the vertical distance between the accelerometers will typically be of secondary importance.

C. Analytical CRBs

To gain some insight into how the estimation accuracy depends on the vehicle dynamics, let us consider the case where the vehicle's angular velocity and angular acceleration can be assumed to be known. Since all gyroscopes measure the same angular velocity, this is usually a feasible approximation for sensor setups with a large number of IMUs [36]. In addition, it is assumed that the estimation procedure has been preceded by a bias calibration. Hence, we may disregard all bias terms. Under these assumptions, the measurement equation providing information about $\mathbf{r}$ at a given sampling instance can be written as

$$\mathbf{y}_a = \mathbf{H}_a \mathbf{r} + \boldsymbol{\epsilon}_a. \tag{12}$$

Here, we have defined $\mathbf{y}_a \triangleq \left[(\delta\tilde{\mathbf{a}}^{(2)})^\intercal \ \ \ldots \ \ (\delta\tilde{\mathbf{a}}^{(N)})^\intercal\right]^\intercal$ and $\mathbf{H}_a \triangleq \mathbf{I}_{N-1} \otimes \boldsymbol{\Omega}_a$, where the angular acceleration tensor is $\boldsymbol{\Omega}_a \triangleq [\boldsymbol{\omega}]^\times [\boldsymbol{\omega}]^\times + [\boldsymbol{\alpha}]^\times$. Moreover, the covariance of $\boldsymbol{\epsilon}_a$ is given by $\mathbf{R}_a \triangleq \sigma_a^2 \bar{\mathbf{I}}_{N,3}$. Now, assuming that $[\boldsymbol{\omega}]^\times \boldsymbol{\alpha} \neq \mathbf{0}_{3,1}$, the parametric CRB for $\mathbf{r}$ given one observation of $\mathbf{y}_a$ is

$$\text{Cov}(\hat{\mathbf{r}}) \succeq \mathbf{P}_{r,a} \tag{13}$$

where we have used $\mathbf{A} \succeq \mathbf{B}$ to denote that $\mathbf{A} - \mathbf{B}$ is positive semidefinite. The inverse FIM is given by

$$\mathbf{P}_{r,a} = \sigma_a^2 (\mathbf{I}_{N-1} + \mathbb{1}_{N-1}) \otimes (\boldsymbol{\Omega}_a^\intercal \boldsymbol{\Omega}_a)^{-1}. \tag{14}$$

As expected, the bound will typically decrease as the angular velocities and accelerations increase. A derivation of (14) is provided in Appendix A.

Several conclusions can be drawn from the CRB bound presented in (13). First, we note that the estimator performance is independent of the number of accelerometers. This is a consequence of assuming perfect knowledge of angular velocity and acceleration. Under this assumption, each accelerometer only provides information about its own position (relative to the first accelerometer), and so, increasing the total number of accelerometers will not improve the estimates, only increase the dimension of the state vector. Second, we note that the correlation function of the estimated relative positions of two accelerometers in some given direction always is equal to $\sigma_\alpha^2 / \sqrt{2\sigma_\alpha^2 \cdot 2\sigma_\alpha^2} = 1/2$, independent of the vehicle dynamics. In other words, the estimates will always be heavily correlated, and this cannot be mitigated by any choice of vehicle dynamics. Third, we study the variance in the direction that is perpendicular to the angular velocity and angular acceleration. That is, we look at the CRB for the estimates of $r_{\omega_\perp} \triangleq (\boldsymbol{\omega}_\perp)^\intercal \mathbf{r}$, where $\boldsymbol{\omega}_\perp \triangleq [\boldsymbol{\omega}]^\times \boldsymbol{\alpha} / \|[\boldsymbol{\omega}]^\times \boldsymbol{\alpha}\|$. In Appendix B, it is shown that the corresponding Cramér-Rao inequality can be written as

$$\text{Var}(\hat{r}_{\omega_\perp}) \geq \frac{2\sigma_a^2}{(\sin(\theta)\|\boldsymbol{\alpha}\|)^2} \tag{15}$$

where $\theta \triangleq \cos^{-1}(\boldsymbol{\omega}^\intercal \boldsymbol{\alpha} / \|\boldsymbol{\omega}\|\|\boldsymbol{\alpha}\|)$ is the angle between $\boldsymbol{\omega}$ and $\boldsymbol{\alpha}$. As may be realized, (15) indicates that the position estimates, in the direction that is perpendicular to $\boldsymbol{\omega}$ and $\boldsymbol{\alpha}$, get worse as the angular rotations are concentrated to one direction, i.e., when θ tend to zero. This illustrates that the horizontal position estimates benefit from rotations along the roll and pitch axes.

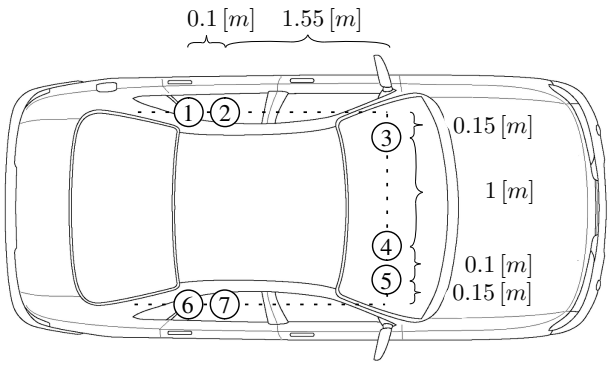

Fig. 4. The placement of the smartphones in the longitudinal and lateral directions of the vehicle frame. For clarity, the figure is not shown in consistent scale.

IV. Field study

The field study used data from the same event as in Section III-B. In addition, the same filter parameters were used. However, instead of using simulations, real-world measurements were employed. As a result, the estimates were affected by several errors that were not modeled in Section II. These include scale factor, cross-coupling, inter-misalignment, and time synchronization errors [22]. Although these error contributions can be expected to degrade the estimation accuracy, the presented framework is still shown to be useful in practical applications.

A. Setup

Data was collected from seven smartphones rigidly attached to the vehicle. The placement of the smartphones is illustrated by Fig. 4. The employed smartphone models where (1) Samsung S3, (2) iPhone 4, (3) Samsung S3, (4) Samsung S3, (5) iPhone 5, (6) Samsung S4, and (7) Samsung S3. The three smartphones in the front seat were placed $0.1\,[m]$ higher up (in the up direction of the vehicle frame) than the four smartphones in the back seat. The relative positions were measured by hand with an uncertainty in the order of $5\,[cm]$ in any given direction. The measurements from different smartphones were time synchronized by the use of GNSS time. In the synchronization, the processing delays for the GNSS

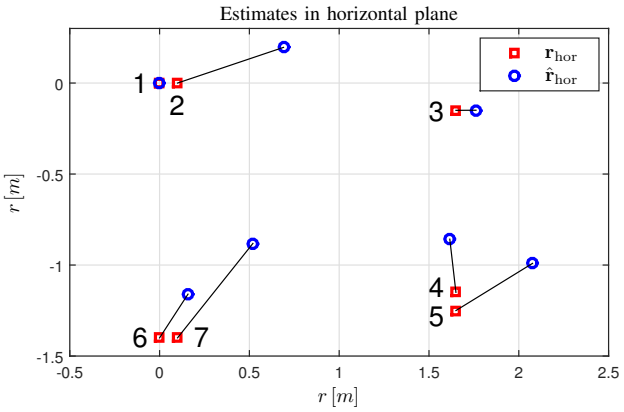

Fig. 5. The estimated and true smartphone positions. All smartphone measurements were processed simultaneously.

receiver and the IMU were assumed to be approximately equal in any single given smartphone. Moreover, all IMU measurements were aligned to the vehicle frame by estimating the smartphone-to-vehicle orientation as described in [37].

B. Results

We now present the results of three experiments. In the first experiment, we attempt to simultaneously estimate the relative positions of the seven smartphones using all available data. The second experiment considers the same problem but with the measurements processed from two smartphones at a time. Last, we study the accuracy of left/right classification by using measurements from two smartphones at a time, and processing the measurements from each cornering maneuver separately.

Defining the origin of the vehicle frame to be at the position of the Samsung S3 denoted by (1) in Fig. 4, Fig. 5 shows the true and estimated relative positions in the horizontal plane after processing all available measurements in the same filter. The true and estimated positions associated with a given smartphone are for visibility connected by a straight black line. Although we are not able to reach the sub-centimeter accuracy that was indicated in Fig. 3 (a), the results are still promising as they show that the overall smartphone geometry is preserved. The horizontal RMSE was $0.46\,[m]$. However, in accordance with what could be expected from the results in Section III-B, the estimates in the up direction (not illustrated by any figure) were worse and had a RMSE of $2.40\,[m]$.

In practice, it is often more relevant to study the accuracy that can be obtained by processing measurements from two smartphones at a time, i.e., when $N = 2$. Fig. 6 shows the relative errors $(\hat{r} - r)/r$ of estimated distances in a given direction (longitudinal or lateral) as dependent on the true distance. Only the cases where the true distance exceeded $0.3\,[m]$ are considered. The measurements were processed from two smartphones at a time, and all 21 possible smartphone combinations were studied (i.e., $\{(1,2),(1,3),\ldots,(1,7),(2,3),(2,4),\ldots,(6,7)\}$). As can be seen, correct left/right or front/back classifications were made in all of the 22 considered cases, i.e., the relative error always exceeded -1. In one case, attributed to the longitudinal distance between the two iPhones, the relative error exceeded

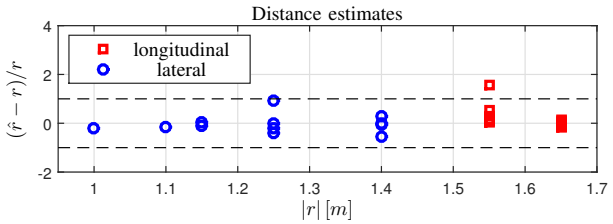

Fig. 6. The relative errors as dependent on the true longitudinal and lateral distance. The measurements were processed from two smartphones at a time.

TABLE II
ACCURACY IN LEFT/RIGHT CLASSIFICATION.

	UKF [%]	Benchmark [16] [%]
$r > 0.3\,[m]$	91.1	88.5
$r < 0.3\,[m]$	50.5	50.5

1. For the cases (not illustrated by any figure) when the true distance was below $0.3\,[m]$, the RMSE was $0.51\,[m]$. Moreover, correct left/right or front/back classifications were made in 7 out of 11 instances (not counting the instances where the true distance was equal to zero).

Last, the proposed framework was benchmarked against the method for left/right classification presented in [16] (the method is detailed in Appendix C). To obtain a sufficient sample size, each of the 32 recorded cornering maneuvers was handled separately. A cornering maneuver was registered whenever the absolute value of the vehicle's angular velocity along the yaw axis exceeded $30\,[^\circ/s]$ and was considered to have ended when then angular velocity fell below $10\,[^\circ/s]$ for at least $0.5\,[s]$. Table II shows the classification accuracy obtained when aggregating the results from all possible smartphone pairs. The results are shown separately for the two cases when the true lateral distance exceeded or fell short of $0.3\,[m]$. In the latter case, neither of the methods perform better than random guessing. However, for larger lateral distances, both methods reach a classification accuracy of about $90\,\%$, with the UKF performing marginally better.

V. SUMMARY

We have presented an IMU-based method for positioning a smartphone with respect to a vehicle. The problem was formulated as a nonlinear filtering problem, where the vehicle dynamics and the sensor biases where treated as nuisance parameters. While previous studies on smartphone-to-vehicle positioning always have estimated the lateral and longitudinal distances separately, this study employed three-dimensional kinematics, thereby enabling the smartphone's position to be estimated jointly in all directions. Moreover, analytical CRBs were derived, and the system model was motivated by observability arguments. As was confirmed by both simulations and real-world experiments, the estimates in the horizontal directions of the vehicle frame will typically be better than in the up direction.

Real-world measurements were employed in three experiments. Simultaneously processing measurements from seven

different smartphones gave a horizontal RMSE in the order of $0.5\,[m]$. When processing measurements from two smartphones at a time, correct left/right or front/back classifications were made in all of the 22 considered cases. Studying each cornering maneuver independently, correct left/right classifications were made in about 90% of the cases when the lateral distance between the devices exceeded $0.3\,[m]$. To summarize, the proposed method enables accurate smartphone-to-vehicle positioning with minimal requirements on vehicle infrastructure. As such, it can be expected to find use in both smartphone-based insurance telematics and distracted driving solutions. Future work should focus on how to incorporate information from human motions and GNSS measurements in a robust manner, and how to handle situations when the smartphones' positions change with time.

APPENDIX A

This appendix derives the CRB in (13). Equation (12) describes a standard linear measurement equation with normally distributed errors and an invertible measurement matrix $\mathbf{H}_a$. Under these conditions, the inverse FIM can be expressed as [38]

$$\begin{aligned}\mathbf{P}_{r,a} &= \mathbf{H}_a^{-1}\mathbf{R}_a(\mathbf{H}_a^\intercal)^{-1} \\ &= \sigma_a^2(\mathbf{I}_{N-1}\otimes\mathbf{\Omega}_a)^{-1}((\mathbf{I}_{N-1}+\mathbb{1}_{N-1})\otimes\mathbf{I}_3) \\ &\quad\cdot((\mathbf{I}_{N-1}\otimes\mathbf{\Omega}_a)^\intercal)^{-1} \\ &= \sigma_a^2(\mathbf{I}_{N-1}\otimes\mathbf{\Omega}_a^{-1})((\mathbf{I}_{N-1}+\mathbb{1}_{N-1})\otimes\mathbf{I}_3) \\ &\quad\cdot(\mathbf{I}_{N-1}\otimes(\mathbf{\Omega}_a^\intercal)^{-1}) \\ &= \sigma_a^2((\mathbf{I}_{N-1}+\mathbb{1}_{N-1})\otimes\mathbf{\Omega}_a^{-1})(\mathbf{I}_{N-1}\otimes(\mathbf{\Omega}_a^\intercal)^{-1}) \\ &= \sigma_a^2(\mathbf{I}_{N-1}+\mathbb{1}_{N-1})\otimes(\mathbf{\Omega}_a^\intercal\mathbf{\Omega}_a)^{-1}\end{aligned} \tag{16}$$

and we are done. Here, it has been used that $(\mathbf{A}\otimes\mathbf{B})^\intercal = \mathbf{A}^\intercal\otimes\mathbf{B}^\intercal$, $(\mathbf{A}\otimes\mathbf{B})\otimes(\mathbf{A}'\otimes\mathbf{B}') = (\mathbf{A}\mathbf{A}')\otimes(\mathbf{B}\mathbf{B}')$, and assuming that $\mathbf{A}$ and $\mathbf{B}$ are nonsingular, $(\mathbf{A}\otimes\mathbf{B})^{-1} = \mathbf{A}^{-1}\otimes\mathbf{B}^{-1}$, for any matrices $\mathbf{A},\mathbf{B},\mathbf{A}'$, and $\mathbf{B}'$ of appropriate dimensions [39].

APPENDIX B

In the following, we derive the CRB in (15). Using that [40]

$$\mathbf{\Omega}_a^{-1} \triangleq \frac{(\boldsymbol{\omega}\boldsymbol{\omega}^\intercal)^2 + \boldsymbol{\alpha}\boldsymbol{\alpha}^\intercal - \left[[\boldsymbol{\omega}]^\times[\boldsymbol{\omega}]^\times\boldsymbol{\alpha}\right]^\times}{\boldsymbol{\alpha}^\intercal[\boldsymbol{\omega}]^\times[\boldsymbol{\omega}]^\times\boldsymbol{\alpha}} \tag{17}$$

it can from (13) be seen that

$$\begin{aligned}\mathrm{Var}(\hat{r}_{\omega_\perp}) &\geq 2\sigma_a^2(\boldsymbol{\omega}_\perp)^\intercal(\mathbf{\Omega}_a^\intercal\mathbf{\Omega}_a)^{-1}\boldsymbol{\omega}_\perp \\ &= -2\sigma_a^2(\boldsymbol{\omega}_\perp)^\intercal\left(\frac{\left[[\boldsymbol{\omega}]^\times[\boldsymbol{\omega}]^\times\boldsymbol{\alpha}\right]^\times}{\boldsymbol{\alpha}^\intercal[\boldsymbol{\omega}]^\times[\boldsymbol{\omega}]^\times\boldsymbol{\alpha}}\right)^2\boldsymbol{\omega}_\perp \\ &= 2\sigma_a^2\frac{(\sin(\theta)\|\boldsymbol{\omega}\|^2\|\boldsymbol{\alpha}\|)^2}{(\sin(\theta)\|\boldsymbol{\omega}\|\|\boldsymbol{\alpha}\|)^4} \\ &= \frac{2\sigma_a^2}{(\sin(\theta)\|\boldsymbol{\alpha}\|)^2}\end{aligned} \tag{18}$$

where we have used that $(\boldsymbol{\omega}_\perp)^\intercal\boldsymbol{\omega}_\perp = 1$ and that $\|[\boldsymbol{\omega}]^\times\boldsymbol{\alpha}\| = \sin(\theta)\|\boldsymbol{\omega}\|\|\boldsymbol{\alpha}\|$.

APPENDIX C

Here, we outline the method for left/right classification [16] of two smartphones that was used as a benchmark in Section IV-A. Making the approximation that the angular velocity is constant and only nonzero along the yaw axis of the vehicle frame, we may, without loss of generality, use that $\boldsymbol{\omega} \approx \omega[0\ \ 0\ \ 1]^\intercal$ and $\boldsymbol{\alpha} \approx \mathbf{0}_{3,1}$. Inserting this into (1) then yields the scalar equation

$$a_{lat}^{(n)} \approx a_{lat}^{(1)} - \omega^2 r_{lat}^{(n)} \tag{19}$$

where $(\cdot)_{lat}$ denotes quantities in the lateral direction of the vehicle frame. Now, using (19) in the limit of $\omega \to 0$, we first estimate the relative accelerometer bias as the constant

$$\delta\hat{b}_{a,lat}^{(n)} = \sum_{|\tilde{\omega}_k|<\gamma} \tilde{a}_{lat,k}^{(n)} - \tilde{a}_{lat,k}^{(1)} \tag{20}$$

where γ is some chosen threshold. Finally, the classification is made based on the sign of the test statistic

$$\hat{r}_{lat}^{(n)} = \sum_{k=N_\omega-N'}^{N_\omega+N'} \tilde{a}_{lat,k}^{(n)} - \tilde{a}_{lat,k}^{(1)} - \delta\hat{b}_{a,lat}^{(n)}. \tag{21}$$

Here, N_ω is the sampling index where $|\tilde{\omega}_k|$ reaches it maximum, and N' is some chosen integer. In section IV-A we used $\gamma = 10\,[^\circ/s]$ and choose N' so that the sum in (21) was taken over samples from an interval of length $1\,[s]$.

REFERENCES

[1] X. Niu, Q. Zhang, Y. Li, Y. Cheng, and C. Shi, "Using inertial sensors of iPhone 4 for car navigation," in *Proc. IEEE/ION Symp. Position Location and Navigation*, Myrtle Beach, SC, Apr. 2012, pp. 555–561.

[2] R. Ansar, P. Sarampakhul, S. Ghosh, N. Mitrovic, M. Asif, J. Dauwels, and P. Jaillet, "Evaluation of smart-phone performance for real-time traffic prediction," in *Proc. IEEE 17th Int. Conf. Intell. Transport. Syst.*, Qingdao, China, Oct. 2014, pp. 3010–3015.

[3] M. Yaqub and I. Gondal, "Smart phone based vehicle condition monitoring," in *Proc. IEEE 8th Int. Conf. Ind. Electron. Appl.*, Melbourne, Australia, Jun. 2013, pp. 267–271.

[4] W.-J. Guan and L.-K. Chen, "Development of advanced driver assist systems using smart phones," in *Proc. IEEE Int. Conf. Advanced Robot. and Intell. Syst.*, Taipei, Taiwan, Jun. 2014, pp. 176–181.

[5] M. Liu, "A study of mobile sensing using smartphones," *Int. J. Distrib. Sensor Netw.*, Jan. 2013.

[6] P. Händel, I. Skog, J. Wahlström, F. Bonawiede, R. Welch, J. Ohlsson, and M. Ohlsson, "Insurance telematics: Opportunities and challenges with the smartphone solution," *IEEE Intell. Transport. Syst. Mag.*, vol. 6, no. 4, pp. 57–70, Oct. 2014.

[7] J. Engelbrecht, M. J. Booysen, G.-J. van Rooyen, and F. J. Bruwer, "Survey of smartphone-based sensing in vehicles for intelligent transportation system applications," *IET Intell. Transport. Syst.*, Jul. 2015.

[8] J. Yang, S. Sidhom, G. Chandrasekaran, T. Vu, H. Liu, N. Cecan, Y. Chen, M. Gruteser, and R. P. Martin, "Sensing driver phone use with acoustic ranging through car speakers," *IEEE Trans. Mobile Comput.*, vol. 11, no. 9, pp. 1426–1440, Sep. 2012.

[9] J. Yang, S. Sidhom, G. Chandrasekaran, T. Vu, H. Liu, N. Cecan, Y. Chen, M. Gruteser, and R. P. Martin, "Detecting driver phone use leveraging car speakers," in *Proc. 17th Annu. Int. Conf. Mobile Comput. Netw.*, Las Vegas, NV, Sep. 2011, pp. 97–108.

[10] M. Feld, T. Schwartz, and C. Muller, "This is me: Using ambient voice patterns for in-car positioning," in *Ambient Intelligence*. Springer Berlin Heidelberg, 2010, pp. 290–294.

[11] H. Chu, V. Raman, J. Shen, A. Kansal, V. Bahl, and R. R. Choudhury, "I am a smartphone and I know my user is driving," in *Proc. 6th Int. Conf. Commun. Syst. Netw.*, Bangalore, India, Jan. 2014.

[12] C. Bo, X. Jian, and X. Li, "TEXIVE: detecting drivers using personal smart phones by leveraging inertial sensors," *CoRR*, vol. abs/1307.1756, 2013.

[13] J. Wahlström, I. Skog, and P. Händel, "Driving behavior analysis for smartphone-based insurance telematics," in *Proc. 2nd Workshop on Physical Analytics*, Florence, Italy, May 2015, pp. 19–24.

[14] C. Miyajima, Y. Nishiwaki, K. Ozawa, T. Wakita, K. Itou, K. Takeda, and F. Itakura, "Driver modeling based on driving behavior and its evaluation in driver identification," *Proc. IEEE*, vol. 95, no. 2, pp. 427–437, Feb. 2007.

[15] Z. He, J. Cao, X. Liu, and S. Tang, "Who sits where? Infrastructure-free in-vehicle cooperative positioning via smartphones," *Sensors*, vol. 14, no. 7, pp. 11 605–11 628, Jun. 2014.

[16] Y. Wang, J. Yang, H. Liu, Y. Chen, M. Gruteser, and R. P. Martin, "Sensing vehicle dynamics for determining driver phone use," in *Proc. 11th Annu. Int. Conf. Mobile Systems, Appl., Services*, Taipei, Taiwan, Jun. 2013, pp. 41–54.

[17] P. Händel, J. Ohlsson, M. Ohlsson, I. Skog, and E. Nygren, "Smartphone-based measurement systems for road vehicle traffic monitoring and usage-based insurance," *IEEE Syst. J.*, vol. 8, no. 4, pp. 1238 – 1248, Dec. 2014.

[18] M. Perlmutter and L. Robin, "High-performance, low cost inertial MEMS: A market in motion!" in *Proc. IEEE/ION Symp. Position Location and Navigation*, Myrtle Beach, SC, Apr. 2012, pp. 225–229.

[19] S. Reddy, M. Mun, J. Burke, D. Estrin, M. Hansen, and M. Srivastava, "Using mobile phones to determine transportation modes," *ACM Trans. Sen. Netw.*, vol. 6, no. 2, pp. 13:1–13:27, 2010.

[20] M. Reininger, S. Miller, Y. Zhuang, and J. Cappos, "A first look at vehicle data collection via smartphone sensors," in *Proc. IEEE Symp. Sensors Appl.*, Zadar, Croatia, Apr. 2015, pp. 1–6.

[21] D. Christin, A. Reinhardt, S. S. Kanhere, and M. Hollick, "A survey on privacy in mobile participatory sensing applications," *J. Syst. Softw.*, vol. 84, no. 11, pp. 1928–1946, Nov. 2011.

[22] P. D. Groves, *Principles of GNSS, inertial, and multisensor integrated navigation systems*, 1st ed. Artech House, 2008.

[23] D. Simon, *Optimal State Estimation*. Wiley, 2006.

[24] S. J. Julier and J. K. Uhlmann, "A new extension of the Kalman filter to nonlinear systems," in *AeroSense*, Orlando, FL, 1997, pp. 182–193.

[25] J. Mendel, "Computational requirements for a discrete Kalman filter," *IEEE Trans. Autom. Control*, vol. 16, no. 6, pp. 748–758, Dec. 1971.

[26] A. P. Miettinen and J. K. Nurminen, "Energy efficiency of mobile clients in cloud computing," in *Proc. 2nd USENIX Conf. Hot Topics Cloud Comput.*, Boston, MA, 2010, pp. 4–11.

[27] T. B. Schön, F. Gustafsson, and P.-J. Nordlund, "Marginalized particle filters for mixed linear/nonlinear state-space models," *IEEE, Trans. Signal Process.*, vol. 53, no. 7, pp. 2279–2289, Jul. 2005.

[28] S. M. Kay, *Fundamentals of Statistical Signal Processing: Detection Theory*. Prentice-Hall, 1998.

[29] O. Hlinka, F. Hlawatsch, and P. Djuric, "Distributed particle filtering in agent networks: A survey, classification, and comparison," *IEEE Signal Process. Mag.*, vol. 30, no. 1, pp. 61–81, Jan. 2013.

[30] I. Rhee, M. Abdel-Hafez, and J. Speyer, "Observability of an integrated GPS/INS during maneuvers," *IEEE Trans. Aerosp. Electron. Syst.*, vol. 40, no. 2, pp. 526–535, Apr. 2004.

[31] J. L. Crassidis and J. L. Junkins, *Optimal Estimation of Dynamic Systems*, 2nd ed. Chapman & Hall/CRC Press, 2012.

[32] N. Bergman and L. Ljung, "Point-mass filter and Cramer-Rao bound for terrain-aided navigation," in *Proc. 36th IEEE Int. Conf. Decision and Control*, San Diego, CA, Dec. 1997, pp. 565–570.

[33] N. Bergman, "Recursive Bayesian estimation - Navigation and tracking applications," Ph.D. dissertation, Linköping University, May 1999.

[34] J.-O. Nilsson, I. Skog, and P. Handel, "Aligning the forces - eliminating the misalignments in IMU arrays," *IEEE Trans. Instrum. Meas.*, vol. 63, no. 10, pp. 2498–2500, Oct. 2014.

[35] X. Niu, Q. Wang, Y. Li, Q. Li, and J. Liu, "Using inertial sensors in smartphones for curriculum experiments of inertial navigation technology," *Educ. Sci.*, vol. 5, no. 1, p. 26, Mar. 2015.

[36] P. Schopp, L. Klingbeil, C. Peters, and Y. Manoli, "Design, geometry evaluation, and calibration of a gyroscope-free inertial measurement unit," *Sensors and Actuators A: Physical*, vol. 162, no. 2, pp. 379 – 387, 2010.

[37] J. Wahlström, I. Skog, and P. Händel, "IMU alignment for smartphone-based automotive navigation," in *Proc. 18th IEEE Int. Conf. Inf. Fusion*, Washington, DC, Jul. 2015, pp. 1437–1443.

[38] S. M. Kay, *Fundamentals of Statistical Signal Processing: Estimation Theory*. Prentice-Hall, Inc., 1993.

[39] R. A. Horn and C. R. Johnson, *Topics in Matrix Analysis*. Cambridge University Press, 1991.

[40] D. Condurache and M. Matcovschi, "Computation of angular velocity and acceleration tensors by direct measurements," *Acta Mechanica*, vol. 153, no. 3-4, pp. 147–167, 2002.

Johan Wahlström received his MSc degree in Engineering Physics from the KTH Royal Institute of Technology, Stockholm, Sweden, in 2014. He subsequently joined the Signal Processing Department at KTH, working towards his PhD. His main research topic is insurance telematics. In 2015, he received a scholarship from the Sweden-America foundation and spent six months at Washington University, St. Louis, USA.

Isaac Skog (S'09-M'10) received the BSc and MSc degrees in Electrical Engineering from the KTH Royal Institute of Technology, Stockholm, Sweden, in 2003 and 2005, respectively. In 2010, he received the Ph.D. degree in Signal Processing with a thesis on low-cost navigation systems. In 2009, he spent 5 months at the Mobile Multi-Sensor System research team, University of Calgary, Canada, as a visiting scholar and in 2011 he spent 4 months at the Indian Institute of Science (IISc), Bangalore, India, as a visiting scholar. He is currently a Researcher at KTH coordinating the KTH Insurance Telematics Lab. He was a recipient of a Best Survey Paper Award by the IEEE Intelligent Transportation Systems Society in 2013.

Peter Händel (S'88-M'94-SM'98) received a Ph.D. degree from Uppsala University, Uppsala, Sweden, in 1993. From 1987 to 1993, he was with Uppsala University. From 1993 to 1997, he was with Ericsson AB, Kista, Sweden. From 1996 to 1997, he was a Visiting Scholar with the Tampere University of Technology, Tampere, Finland. Since 1997, he has been with the KTH Royal Institute of Technology, Stockholm, Sweden, where he is currently a Professor of Signal Processing and the Head of the Department of Signal Processing. From 2000 to 2006, he held an adjunct position at the Swedish Defence Research Agency. He has been a Guest Professor at the Indian Institute of Science (IISc), Bangalore, India, and at the University of Gävle, Sweden. He is a co-founder of Movelo AB. Dr. Händel has served as an associate editor for the IEEE TRANSACTIONS ON SIGNAL PROCESSING. He was a recipient of a Best Survey Paper Award by the IEEE Intelligent Transportation Systems Society in 2013.

Arye Nehorai (S'80–M'83–SM'90–F'94) is the Eugene and Martha Lohman Professor and Chair of the Preston M. Green Department of Electrical and Systems Engineering (ESE), Professor in the Department of Biomedical Engineering (by courtesy) and in the Division of Biology and Biomedical Studies (DBBS) at Washington University in St. Louis (WUSTL). He serves as the Director of the Center for Sensor Signal and Information Processing at WUSTL. Under his leadership as department chair, the undergraduate enrollment has more than tripled in the last four years. Earlier, he was a faculty member at Yale University and the University of Illinois in Chicago. He received both B.Sc. and M.Sc. degrees from the Technion, Israel and a Ph.D. from Stanford University, California.

Dr. Nehorai served as Editor-in-Chief of the *IEEE Transactions on Signal Processing* from 2000 to 2002. From 2003 to 2005 he was the Vice President (Publications) of the IEEE Signal Processing Society (SPS), the Chair of the Publications Board, and a member of the Executive Committee of this Society. He was the founding editor of the special columns on Leadership Reflections in the *IEEE Signal Processing Magazine* from 2003 to 2006.

Dr. Nehorai received the 2006 IEEE SPS Technical Achievement Award and the 2010 IEEE SPS Meritorious Service Award. He was elected Distinguished Lecturer of the IEEE SPS for a term lasting from 2004 to 2005. He received several best paper awards in IEEE journals and conferences. In 2001 he was named University Scholar of the University of Illinois. Dr. Nehorai was the Principal Investigator of the Multidisciplinary University Research Initiative (MURI) project entitled Adaptive Waveform Diversity for Full Spectral Dominance from 2005 to 2010. He has been a Fellow of the IEEE since 1994, a Fellow of the Royal Statistical Society since 1996, and a Fellow of AAAS since 2012.